Salt intrusion dynamics in a well-mixed sub-estuary connected to a partially to well-mixed main estuary

Zhongyuan Lin[c,d], Guang Zhang[a,b], Huazhi Zou[c,d], Wenping Gong[a,b*]

[a]School of Marine Sciences, Sun Yat-sen University, Zhuhai, 519082, China

[b]Guangdong Provincial Key Laboratory of Marine Resources and Coastal Engineering, Zhuhai, 519082, China

[c] Key Laboratory of Pearl River Estuary Regulation and Protection of Ministry of Water Resource, Guangzhou 510611, China

[d] Pearl River Water Resource Research Institute, Guangzhou 510611, China

Corresponding Author: Wenping Gong (gongwp@mail.sysu.edu.cn)

Abstract

Salt intrusion in estuaries has been exacerbated by climate change and human activities. Previous studies have primarily focused on salt intrusion in the mainstem of estuaries, whereas those in sub-estuaries (those branch off their main estuaries) have received less attention. During an extended La Niña event from 2021 to 2022, a sub-estuary (the East River estuary） alongside the Pearl River Estuary, China, experienced severe salt intrusion, posing a threat to the freshwater supply in the surrounding area. Observations revealed that maximum salinities in the main estuary typically preceded spring tides, exhibiting significant asymmetry in salinity rise and fall over a fortnightly timescale. In contrast, in the upstream region of the sub-estuary, the variation of salinity was in phase with that of the tidal range, and the rise and fall of the salinity ~~rise and fall exhibited~~were more symmetrical.

Inspired by these observations, we employed idealized numerical models and analytical solutions to investigate the underlying physics behind these behaviors. It was

29   discovered that under normal dry condition (with a river discharge of 1500 m^3 s^{-1} at the

30   head of the main estuary), the river-tide interaction and change in horizontal dispersion

31   accounted for the in-phase relationship between the salinity and tidal range in the

32   upstream region of the sub-estuary. Under extremely dry conditions (i.e., a river

33   discharge of 500 m^3 s^{-1} at the head of the main estuary), salinity variations were in-

34   phase with those of the tidal range in the middle as well as the upstream region of the

35   sub-estuary. The variation of salinity in the main estuary, along with those of salt

36   dispersion and freshwater influx inside the sub-estuary collectively influenced salinity

37   variation in the well-mixed sub-estuary. These findings have important implications for

38   water resource management and salt intrusion prevention in the catchment area.

40

41   **1. Introduction**
42

43   Salt intrusion in estuaries has emerged as an increasingly significant

44   environmental issue, as it contaminates water quality, restricts freshwater supply, and

45   affects the biota's habitat in estuaries (Payo-Payo et al., 2022). The severity of salt

46   intrusion in estuaries has been further exacerbated by both climate change and

47   anthropogenic activities. Climate change has led to more severe droughts in various

48   regions worldwide (Spinoni et al., 2014), resulting in reduced freshwater flow from

49   upstream watershed basin into estuaries. In turn, this has intensified salt intrusion in

50   these areas. Additionally, sea level rise has been identified as a contributing factor to

51 this phenomenon (e.g., Hong et al., 2020). Human activities, including dam

52 construction in the watershed, channel dredging, and land reclamation in estuaries, have

53 caused reductions in river inflow, channel deepening, and enhanced convergence of

54 estuarine geometry, all of which favor an increase in salt intrusion (e.g., Ralston and

55 Geyer, 2019).

56 Salt intrusion in estuaries is the result of landward salt transport, which consists of

57 steady shear and tidal oscillatory transport (MacCready and Geyer, 2010). The

58 combination of estuarine circulation and salinity stratification induces a steady shear

59 when averaged in a tidal cycle. Tidal oscillatory transport is generated by tidal pumping

60 such as the jet-sink flow for an inlet (Stommel and Farmer, 1952), tidal trapping with a

61 side embayment (Okubo, 1973), tidal shear dispersion by the vertical shears of current

62 and mixing (Bowden, 1965), tidal straining (Simpson et al., 1990), and chaotic stirring

63 (Zimmerman, 1986).

64 In general, for a partially mixed estuary in which the steady shear dominates the

65 landward salt transport, the salt intrusion is strongest during neap tides and weakest

66 during spring tides under the steady-state conditions, meaning that the change in salinity

67 is out-of-phase with that in the tidal range. However, for a well-mixed and/or a salt

68 wedge estuary, in which the tidal dispersion is the dominant contributor to landward

69 salt transport, the salt intrusion is strongest during spring tides and weakest during neap

70 tides, signifying that the salinity variation is in phase with the tidal range (Ralston et

71 al., 2010). These steady-state situations are altered by the unsteadiness of external

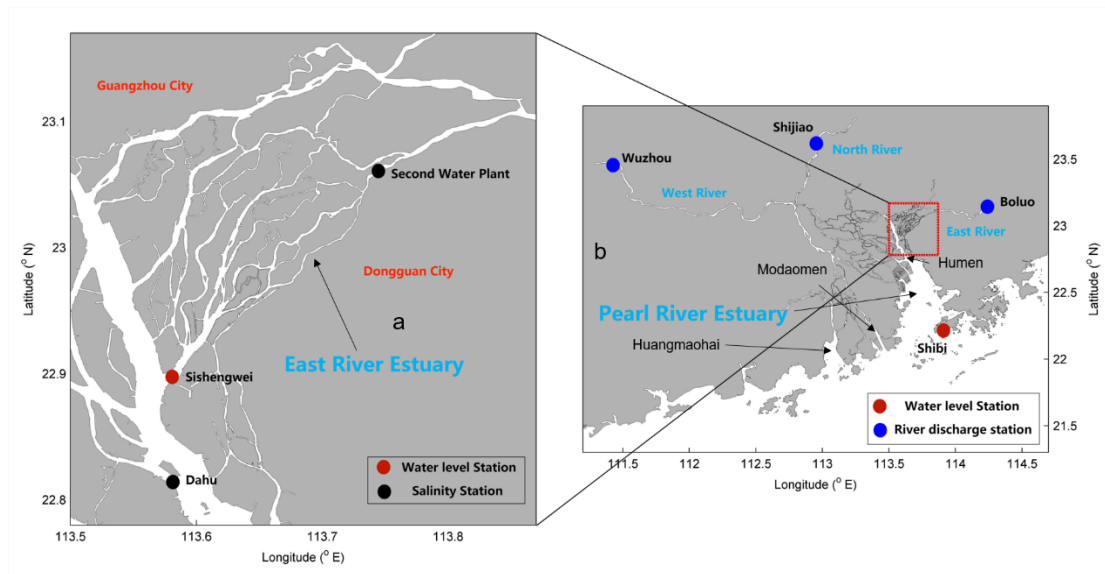72 forcing and the adjustment of estuaries to the changing forcings (Chen 2015 and

73   references therein). In general, when the internal timescale of an estuary, which is

74   defined as the time needed for a water parcel from the upstream to travel through the

75   estuary by the river-induced flow, is shorter than the external timescale, which is often

76   the spring-neap tidal cycle, the salinity variation in an estuary can keep pace with the

77   change in tidal forcing and reaches steady state. However, when the internal timescale

78   is longer than the external timescale, the salt intrusion can hardly reach the steady state,

79   and there exists a phase shift between the salt intrusion and tidal range, such as in the

80   Modaomen estuary (Gong and Shen, 2011) and Hudson River (Bowen and Geyer,

81   2003).

82   Previous studies on salt intrusion have primarily focused on main estuaries, where

83   freshwater discharge empties into the estuarine waterbody at the estuary head and is

84   profoundly diluted by the seawater from the ocean. However, there has been relatively

85   less research on salinity dynamics specifically in tidal creeks or sub-estuaries, i.e. those

86   that reside aside from their main estuary. It is worth noting that larger estuaries often

87   possess sub-estuaries or tidal creeks, as highlighted by Uncles and Stephens (2010).

88   Sub-estuaries branch off the stem of their main estuary and exhibit behavior that is

89   partially dependent on processes acting within the main estuary. Haywood et al. (1982)

90   described the importance of conditions at the confluence of the York River sub-estuary

91   and the Chesapeake Bay to salinity stratification within the sub-estuary. Uncles and

92   Stephens (2010) investigated the salinity dynamics in a sub-estuary (Tavy) connected

93   to the main estuary (Tamar, UK). They noted that the tidal range had a limited effect on

94   the salinity in the sub-estuary. Yellen et al. (2017) examined the sediment dynamics in

a side embayment of the main estuary of Connecticut, USA, and found that salinity

intrusion from the main estuary enhanced sediment trapping inside the sub-estuary.

The previous studies on sub-estuary salt dynamics have mainly focused on

examining salinity variabilities and water column stratification, as exemplified by the

work of Haywood et al. (1982). Some investigations have also explored the influence

of river discharge from the heads of the main estuary and sub-estuary, as well as the

impact of winds, as discussed by Uncles and Stephens (2010). However, there remains

a knowledge gap regarding how the salt dynamics in the main estuary affect those in

the sub-estuary, as well as how the interaction between river flow and tides influences

salinity variations in the sub-estuary. Regarding the river-tide interaction, here we focus

on how tides affect river flow through mechanisms such as nonlinear bottom friction

and advective terms in the momentum equation, as outlined by Buschman et al. (2009),

whereas the effect of river flow on tidal propagation will not be explored.

In 2021, under the influence of a La Nina event, the precipitation in the Pearl River

Delta (PRD) area (Fig. 1), China, was extremely low, and the salt intrusion was very

severe, which imposed a great threat to the freshwater supply in the region, especially

during winter months (December to February). Alongside the Pearl River Estuary

(PRE), a sub-estuary of the East River estuary (Fig. 1), also experienced strong salt

intrusion and heavily impacted the water supply to the city of Dongguan, home to a

population of 10 million people. This shortage of freshwater became a significant

concern for the surrounding people, especially during the Spring Festival, the Chinese

Lunar New Year.

Fig.1. a) The East River estuary; b) Map of the Pearl River Delta and the locations of hydrological and water level stations.

The present work has two objectives: (a) to investigate the characteristics of salt intrusion in a well-mixed sub-estuary by analyzing observation data. The characteristics include spatial-temporal variations of salt intrusion and its relationship with river flow and tidal range; (b) to explore the underlying physics behind salt intrusion in the sub-estuary, such as the impacts of salt dynamics in the main estuary, and the river-tide interaction inside the sub-estuary. To achieve the above goals, we first collected and analyzed observational data of salt intrusion at the East River estuary. Then we utilized an idealized configuration for numerical model investigation. Two numerical model experiments with mean and extremely low river discharges in dry seasons in the main estuary, respectively, were conducted to identify the relevant mechanisms for the variability of salt intrusion in the sub-estuary. Furthermore, to clearly understand the phase relationship between salinity and tidal range, analytical solutions for the subtidal

salinity in the well-mixed sub-estuary were utilized.

The remainder of this paper is structured as follows. The study site is briefly introduced in Section 2. The methods of data analysis, numerical model simulation, and analytical solution are presented in Section 3. In Section 4, the results of the salt intrusion dynamics through the measurement data analysis, numerical model, and analytical solution are demonstrated, followed by some discussions on the impacts of river-tide interaction in the sub-estuary, the salt dynamics in the main estuary, and the limitations of this study in Section 5. Finally, a summary and conclusion are given in Section 6.

2. Study site

The Pearl River, China's second largest river in terms of annual freshwater discharge, has three main branches: West River, North River, and East River (Hu et al., 2011), as displayed in Fig. 1b. The Pearl River forms a complex delta, known as the Pearl River Delta (PRD), which consists of the downstream river network and three estuaries, from west to east: the Huangmaohai Estuary, the Modaomen Estuary, and the PRE (Fig. 1b). The PRE, the largest of the three estuaries, is funnel-shaped and has a mean depth of 4.6 m (Wu et al., 2016). Its width decreases from 50 km at its mouth between Hong Kong and Macau to 6 km at Humen Outlet. The axial length of the estuary from the mouth to Humen is approximately 70 km. Above the Humen, the estuary becomes relatively straight and further extends almost 90 km landward to its head. Upstream of the Humen, there exists a waterway known as Shizhiyang. Along the

156   waterway, there are several river tributaries, among which the East River sub-estuary,

157   are distributed on the east side.

158   The river discharge into the PRE is about 1/4 of the total river flow from the Pearl

159   River. The total annual river discharge of the Pearl River is 3260×10^8 m^3, in which the

160   river discharge experiences distinct seasonal variations. During the dry season (from

161   November to March), the river discharge at the head of the Pearl River takes up only

162   about 30% of the annual discharge, so the total river discharge of the Pearl River is

163   about 6000 m^3/s in the dry season, and the upstream river discharge of the PRE is 1500

164   m^3/s (1/4 of the total). Under extremely dry conditions, the river discharge at the head

165   of the PRE can be less than 1000 m^3/s.

166   The PRE has a microtidal and mixed semi-diurnal regime (Mao et al., 2004). The

167   annual mean tidal range is 1.45 m near Lantau Island (at the mouth of the PRE) and

168   1.77 m near the Humen outlet (Gong et al., 2018). The amplitudes of M_2, S_2, K_1, and O_1

169   constituents near the Lautau Island are 35.5, 14, 33.5, and 27.9 cm, respectively (Mao

170   et al., 2004), showing the dominance of the M_2 constituent. The alternation of neap and

171   spring tides causes the tidal range near Lantau Island to vary from approximately 0.7 m

172   during neap tides to approximately 2 m during spring tides. Apart from the fortnightly

173   variation of the tidal range, there also exists a monthly variation, which is referred to as

174   the apogee/perigee cycle (Payo-Payo et al., 2022).

175   The PRE exhibits strong seasonal variation and is highly stratified during the wet

176   summer season (July to September), with the bottom isohaline of 10 ~~psu~~psu protruding

177   into the upper estuary (50 to 70 km from the estuary mouth) and the surface isohaline

178 of 10 ~~psu~~psu extending outside of the estuary. The subtidal bottom-surface salinity

179 difference is mostly greater than 10 ~~psu~~psu inside the estuary (Dong et al., 2004).

180 During the dry season, the PRE is generally in a partially mixed state, with the bottom

181 isohaline of 10 ~~psu~~psu reaching the Humen Outlet, and the surface isohaline of 10

182 ~~psu~~psu lying in the upper estuary (Wong et al., 2003; Gong et al., 2018). In the dry

183 season, the horizontal difference of depth-mean salinity varies by between 20 and 25

184 ~~psu~~psu across a distance of 70 km from the estuary mouth to Humen Outlet, and the

185 vertical salinity difference between the surface and bottom varies from 1 to 12 ~~psu~~psu

186 along the channels in the estuary.

187 The East River is a branch of the Pearl River, with a length of 562 km and a

188 drainage area of 27,040 km^2. It forms a sub-delta, known as the East River Delta, which

189 is located on the east side of the PRE and above the Humen Outlet (Fig. 1a). The upper

190 reach of the East River is essentially composed of a single channel, while in its lower

191 reach, downstream of Dongguan City, a complex river network is formed, including

192 several tributaries (Fig. 1a). Here we focus on the southernmost tributary, which merges

193 into the main estuary at the confluence of Sishengwei, where a hydrological station

194 resides. This tributary has a length of approximately 75 km from the confluence

195 (Sishengwei) to the upstream hydrological station of Boluo (Fig. 1b), and a mean water

196 depth of less than 5 m.

197 The average annual freshwater load of the East River is 240×10^8 m^3, or a mean

198 river discharge of 728 m^3 s^{-1}, accounting for 7.1% of the total river flow of the Pearl

199 River. During dry seasons, the river discharge is approximately 400 m^3 s^{-1}. However,

the annual mean river discharge in 2021 was only 262 $m^3 s^{-1}$. During the winter of 2021, the salinity at several water plants exceeded the drinking water criteria of 0.5 ~~psu~~psu for a lasting duration of 3 months and impaired the freshwater supply in the region.

Similar to the main estuary, the tidal regime in the East River sub-estuary is a mixed semi-diurnal one, with the tidal range decreasing when propagating upstream due to the predominance of the bottom friction over the estuarine convergence. In recent decades, the tidal strength has been seen to increase by human activities, such as sand mining in the estuary (Jia et al., 2006).

3. Methods

3.1 Observation data and analysis

The observation data here consist of the daily discharge of the West, North, and East Rivers, hourly water level data at the confluence (Sishengwei) between the East River sub-estuary and the main estuary (PRE), daily sea level at the mouth of the PRE (Shibi), and hourly surface salinity data at the Dahu station, which is located downstream of the Sishengwei, and at the Second Water Plant of Dongguan City. These two stations span a distance of approximately 30 km. The river discharge data at three river branches of the Pearl River, hourly water level data at Sishengwei, and hourly surface salinity data at Dahu are from the Pearl River Water Resources Commission, whereas the salinity data at the Second Water Plant is from the Water Authority of Dongguan City. The sea level data at the estuary mouth is from the Hong Kong

223   Observatory (http://gb.weather.gov.hk/contentc.htm). All the salinity data are the

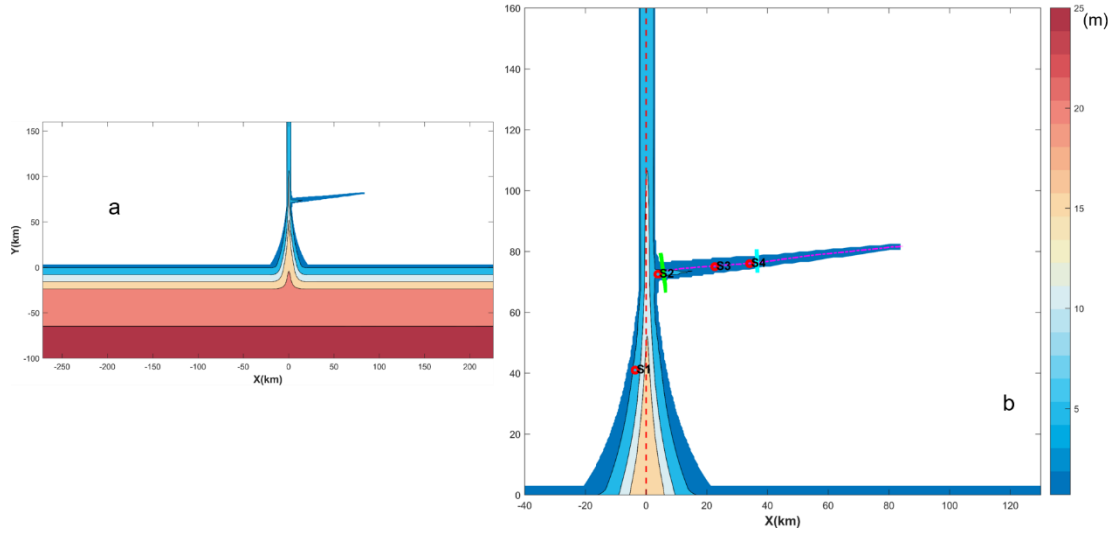224   surface salinities.

225   The salinity data at the Second Water Plant was subject to wavelet analysis, a

226   method that has been widely used to analyze geophysical data, like in salt intrusion

227   studies in estuaries (Liu et al., 2014; Gong et al., 2022). This method can identify

228   localized periodicities (or bands) that are linked to specific processes, such as tidal and

229   spring-neap variations. In this study, the continuous wavelet transform (CWT) method

230   was used to identify the multi-scale characteristics of salinity, and cross wavelet was

231   employed to examine the nonlinear correlations among variables, such as between the

232   salinity of the Second Water Plant and the water level at Sishengwei, between the

233   salinity of the Second Water Plant and the salinity of Dahu, and between the salinity of

234   the Second Water Plant and the river discharge at the Boluo Station.

235

3.2 Numerical model configuration and experiments

237

238   The Regional Ocean Modeling System (ROMS) was used in this modeling study.

239   ROMS is a free-surface, hydrostatic, primitive-equations ocean model that uses

240   stretched, terrain-following vertical coordinates and orthogonal curvilinear horizontal

241   coordinates on an Arakawa C-grid (Haidvogel et al. 2000). The model domain was

242   designed as an estuary-shelf system (Fig. 2). In the coordinate system, x is in the

243

Fig. 2. Geometry and bathymetry of the idealized model domain: a)for the whole domain;

b)zoom in for the area of concern. The origin of the coordinates is in the middle of the main

estuary mouth. The longitudinal sections in the main and sub-estuary are shown as dashed lines,

and the cross-sections inside the sub-estuary are shown as color solid lines. The locations of

several stations are indicated.

cross-estuary direction, with rightward being positive, y is in the along-channel

direction, with landward being positive, and z directs upward. The origin of the

system is in the middle of the estuary mouth. The estuary is composed of a convergent

part and a straight part. The geometry and bathymetry of the estuary roughly resemble

those of the PRE, with the convergent part extending from the estuary mouth to the

Humen Outlet (70 km in length), and the straight part from the Humen Outlet to the

head of the estuary (90 km long). For the convergent part, the estuarine width B is

assumed to decrease exponentially in the landward direction, as follows:

$$B = B_0 \exp(-\frac{y}{L_b}) \tag{1}$$

where B_0 is the estuarine width at the estuary mouth (here taken as 46 km) and L_b is

the width convergence length (taken as 31 km, as estimated by Zhang et al., 2021). The

bathymetry of the PRE is characterized by deep channels and side shallow shoals.

Following Wei et al. (2017), ~~We~~ we roughly mimicked this feature by setting the

bathymetry of the convergent part as:

$$H(x,y) = H_{min} + (H_m - H_{min})\frac{y}{L} + (H_{max} - H_{min}) \times \left(1 - \frac{y}{L}\right)\left(1 - \frac{4x^2}{B^2}\right)e^{-C_f\left(\frac{4x^2}{B^2}\right)} \quad (2)$$

where L is the length of the convergent part (70 km); H_{max} (20 m) and H_{min} (3.0 m)

are the maximum and minimum water depths at the estuary mouth, the width-averaged

water depth H_m is constant (H_m= 8 m) along the estuary, and the parameter C_f is set

as 4, ~~–~~based on the bathymetry data. In the straight part of the estuary, the bathymetry

was kept the same as that of the uppermost cross-section of the convergent part.

At a distance of 75 km from the mouth of the main estuary, we added a sub-estuary

on the east side, resembling the East River sub-estuary. The sub-estuary extends in a

southwest-northeast direction for a distance of approximately 75 km. The width of the

sub-estuary is mildly convergent, with a width of 10 km at the confluence and

decreasing to 600 m at the head, with an e-folding decrease scale (L_b) of 90 km. The

water depth decreases landward from 6 m at the confluence to 3.5 m at the head of the

sub-estuary.

As the boundary conditions at an estuary mouth are generally unknown, we added

a continental shelf to the model domain. The shelf is 100 km wide and approximately

500 km long, with the downstream part (representing the Kelvin wave propagation

direction) being slightly longer than the upstream part. The water depth of the shelf is

uniform in the alongshore direction and increases linearly from the coast to the offshore

direction, with a slope of 1×10^{-4}. The model grid has 313×506 cells, with a cross-

channel spatial resolution of 300 m and an along-channel resolution of 500 m in the

284   estuary. The horizontal resolution decreases on the shelf and becomes 2 km at the open

285   ocean boundaries. Fifteen vertical s-grid layers were specified with higher resolutions

286   near the surface and bottom, and the coefficients of θ_s, θ_b, and h_c were set as 2.5,

287   3.0, and 5.0, respectively. In ROMS Model, coefficients larger than unity for θ_s, θ_b

288   can generate higher resolutions near the surface and bottom, respectively. For details of

289   these coefficients, ~~the ROMS User manual~~the reference of Shchepetkin and

290   McWilliams (2005) can be referred to.

291   We used the $k - \varepsilon$ submodel of the Generic Length Scale (*GLS*) turbulence

292   closure scheme to calculate the vertical mixing (Umlauf and Burchard, 2003; Warner

293   et al., 2005). The horizontal eddy viscosity and diffusivity were calculated using the

294   Smagorinsky scheme (Smagorinsky, 1963). The bottom friction was calculated based

295   on the log-layer assumption near the bottom, with a bottom roughness length of 1 mm.

296   This setting results in a mean bottom drag coefficient of 0.005. The open ocean

297   boundary condition for the barotropic component consists of a Flather/Chapman

298   boundary condition for the depth-averaged flow and sea surface elevation (Chapman,

299   1985; Flather, 1976). The open boundary conditions for the temperature, salinity, and

300   baroclinic current are the Orlanski-type radiation conditions (Orlanski, 1976).

301   To investigate the impact of salt dynamics in the main estuary on salt intrusion in

302   the sub-estuary, two numerical experiments were implemented. In both cases, the river

303   discharge at the head of the sub-estuary was set as 200 m^3/s, which is approximately

304   the value during the dry season in 2021 in the East River estuary. A time series of water

305   levels produced by a combination of 12 tidal constituents was specified at the offshore

306   boundary. These 12 tidal constituents are M_2, S_2, N_2, K_2, K_1,

307   O_1, P_1, Q_1, M_4, MS_4, M_m, M_f, respectively. The tidal constants of these 12

308 constituents were obtained from the Oregon Tidal Database (OPTS). As the tidal

309 amplitudes are almost doubled at the mouth of the main estuary due to the

310 superimposition of propagating and reflected tidal waves, the amplitudes of these tidal

311 constituents at the offshore boundary were reduced by half. Case 1 was set with a river

312 discharge of 1,500 m^3 s^{-1} at the main estuary's head. The river discharge of 1500 m^3 /s

313 is representative of the total amount that empties into the PRE from different outlets in

314 dry seasons (Gong et al., 2020), being lumped as input at the head of the PRE. The

315 inflowing river water was prescribed to have zero salinity and a temperature of 22℃,

316 identical to the background temperature setting throughout the entire domain. The

317 incoming salinity at the offshore boundary was specified to be 34 ~~psu~~psu. In Case 2,

318 we set an extremely low river discharge (500 m^3 s^{-1}) at the head of the main estuary,

319 which is realistic under the La Nina event. In this scenario, we aimed to check how the

320 salt dynamics in the more mixed main estuary affect the salinity variation in the sub-

321 estuary.

322

323 **3.3 Analytical solutions for the salinity variation in the well-mixed sub-estuary**

324

325   For the subtidal (here is that averaged over 25 hours) salinity variation along the

326 well-mixed sub-estuary, the advection-diffusion equation can be written as:

$$\frac{\partial (A\overline{S})}{\partial t} = -\frac{\partial}{\partial x}\left(A\overline{u}\,\overline{S}\right) + \frac{\partial}{\partial x}\left(AK_x \frac{\partial \overline{S}}{\partial x}\right) \tag{3}$$

328 where A is the cross-sectional area, $\overline{S}$ is the subtidal salinity in the cross-section,

329 t is time, $\overline{u}$ is subtidal longitudinal velocity, x is the distance along the sub-estuary,

330 K_x is the longitudinal dispersion coefficient. The left term in Eq. 3 indicates the local

15

331 acceleration and the unsteadiness of salinity variation. The unsteadiness is controlled

332 by the contrast between the internal and external timescales. The internal timescale of

333 the sub-estuary for a river discharge of 200 m^3/s was estimated to be longer than 30

334 days. This timescale is longer than the fortnightly timescale, and the salinity in the sub-

335 estuary can hardly reach a steady state under the varying tides, thus the time tendency

336 term should not be ignored. Savenije (2012) suggested another timescale to quantify

337 the estuary's response timescale (T_S), which is expressed as:

$$T_S = -\frac{1}{Q_f \overline{S}(X)} \int_X^L A\overline{S}\,dx \qquad\qquad (4)$$

339 Based on the numerical model results, by selecting X at the sub-estuary's mouth,

340 we calculated the response timescale to be 16.22 day, which is comparable to the spring-

341 neap tidal cycle. ~~However, when this term is included in the model, the analytical~~

342 ~~solution of Eq. (3) becomes a little difficult to obtain as the horizontal dispersion is~~

343 ~~time-dependent and varies with the tidal strength.~~This indicates that the salinity

344 variation in the sub-estuary can approximately keep pace with the changing tidal

345 forcing. We ~~simplified this problem by~~thus ignore~~ding~~ the unsteadiness term and

346 ~~assuming~~ assumed that the horizontal dispersion is constant in a subtidal period and

347 scales with the tidal current at the sub-estuary's mouth. Meanwhile, the boundary

348 condition of subtidal salinity at the sub-estuary's mouth was updated at each subtidal

349 period. In this way, the calculation of subtidal salinity in the sub-estuary can be

350 proceeded. As such, Eq. 3 becomes (Cai et al., 2015):

$$\frac{Q}{A}\overline{S} = K_x \frac{\partial \overline{S}}{\partial x} \qquad\qquad (45)$$

352 in which Q is the river discharge. We assume that the cross-sectional area decreases

353   exponentially in the landward, $A = A_0\exp(-x/a)$, where a is the convergence

354   length scale of the cross-sectional area. When the longitudinal dispersion coefficient

355   K_x is assumed to be a constant along the sub-estuary, the subtidal salinity along the

356   sub-estuary can be obtained as:

$$\frac{\bar{S}}{S_0} = \exp\{-\frac{Qa}{A_0 K_x}\left[\exp\left(\frac{x}{a}\right) - 1\right]\}$$ (56)

358   For each subtidal period, we obtained the subtidal salinity (S_0) and the tidal current

359   at the mouth of the sub-estuary from the numerical model results, and related the

360   horizontal dispersion (K_x) to the tidal strength at the mouth. When these data were

361   available, the subtidal salinity at each subtidal period was calculated for our numerical

362   simulation period.

363   When the K_x is assumed to vary along the estuary, the salinity variation along the

364   sub-estuary is in another form and not presented here (Savenije, 2012), as that form of

365   K_x is not related to the tidal strength and is unsuitable for our situation here, so this

366   scenario is not pursued further.

367

368   **3.4 Calculation of the salt and freshwater fluxes**

369

370   The salt flux at a cross-section is calculated as follows:

$$F_s = \int uSdA$$ (67)

372   where u is the instantaneous longitudinal velocity, and S is the instantaneous

373   salinity. The instantaneous flux was integrated and then averaged over a subtidal period

374   (25 hours).

375   As the changes in freshwater transport by the river-tide interaction are concerned,

376   we also calculated the freshwater flux, which is:

$$F_f = \int u(1 - \frac{S}{S_0})dA$$ (78)

17

378 where S_0 is the ocean salinity, here is taken to be 34 ~~psu~~psu. The freshwater flux was

379 also integrated and averaged over a subtidal timescale.
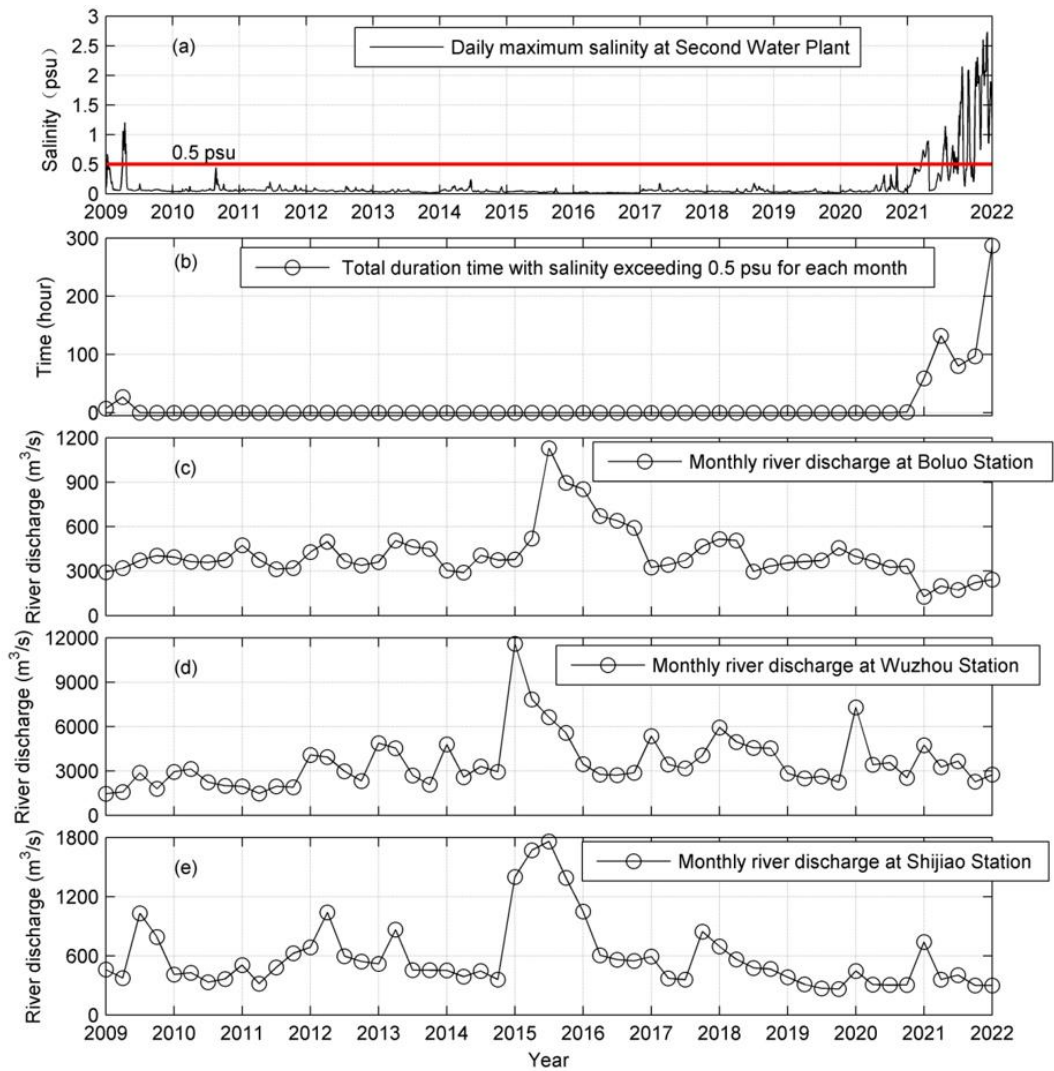
380

381 **4. Results**

382

383 **4.1 The characteristics of salt dynamics in the sub-estuary: based on observation**

384   **data**

385

386   Here we take the Second Water Plant as a representative station in the upstream

387 region of the sub-estuary. The salinity variation at this station was checked from 2009

388 to 2022, as shown in Fig. 3. It indicates (Fig. 3a) that before 2021, the surface salinity

389 was generally lower than 0.5 ~~psu~~psu and suitable for extraction. During the winter

390 season of 2021-2022, the salinity exceeded the drinking water criterion for a prolonged

391 period of 280 hours in January 2022 (Fig. 3b). These elevated salinities coincided with

392 the decreased river discharge from the upstream in the PRD, shown by the data at the

393 hydrological stations of Boluo, Wuzhou and Shijiao (Figs. 3c, 3d and 3e).
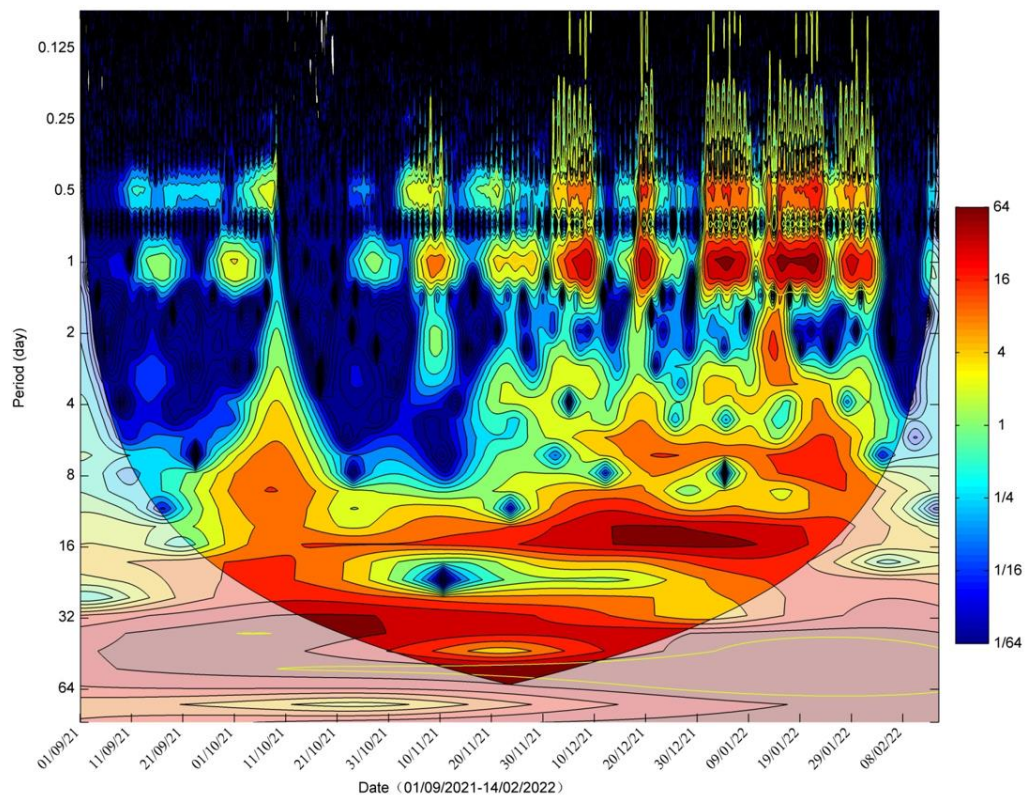
394

Fig.3. Timeseries of: a) Daily maximum salinity at the Second Water Plant; b) Total duration period

with salinity exceeding 0.5 ~~psu~~psu for each month; c) Monthly river discharge at Boluo station

(upstream of the East River); d) Monthly river discharge at Wuzhou station (upstream of the West

River); e) Monthly river discharge at Shijiao station (upstream of the North River). Note that the

river discharges in 2022 are comparable to those of 2009 but the effect on salinities are dramatically

higher.

We conducted wavelet analysis for the salinity data of the Second Water Plant

Station from September 2021 to February 2022, when the salt intrusion was severe. The

result is shown in Fig. 4. It indicates that the power of salinity variations is concentrated

in several periods: one is in the range of 0.5 to 1 day, which is caused by tidal fluctuation;

the second period lies in the range of 5-9 days, which is presumably induced by wind

forcing; the third one is in the range of 14-16 days, obviously by the fortnightly

variation of spring-neap tidal cycle. The last one is within the range of 28 days, near

the monthly timescale. This periodicity should be caused by the tidal beating among

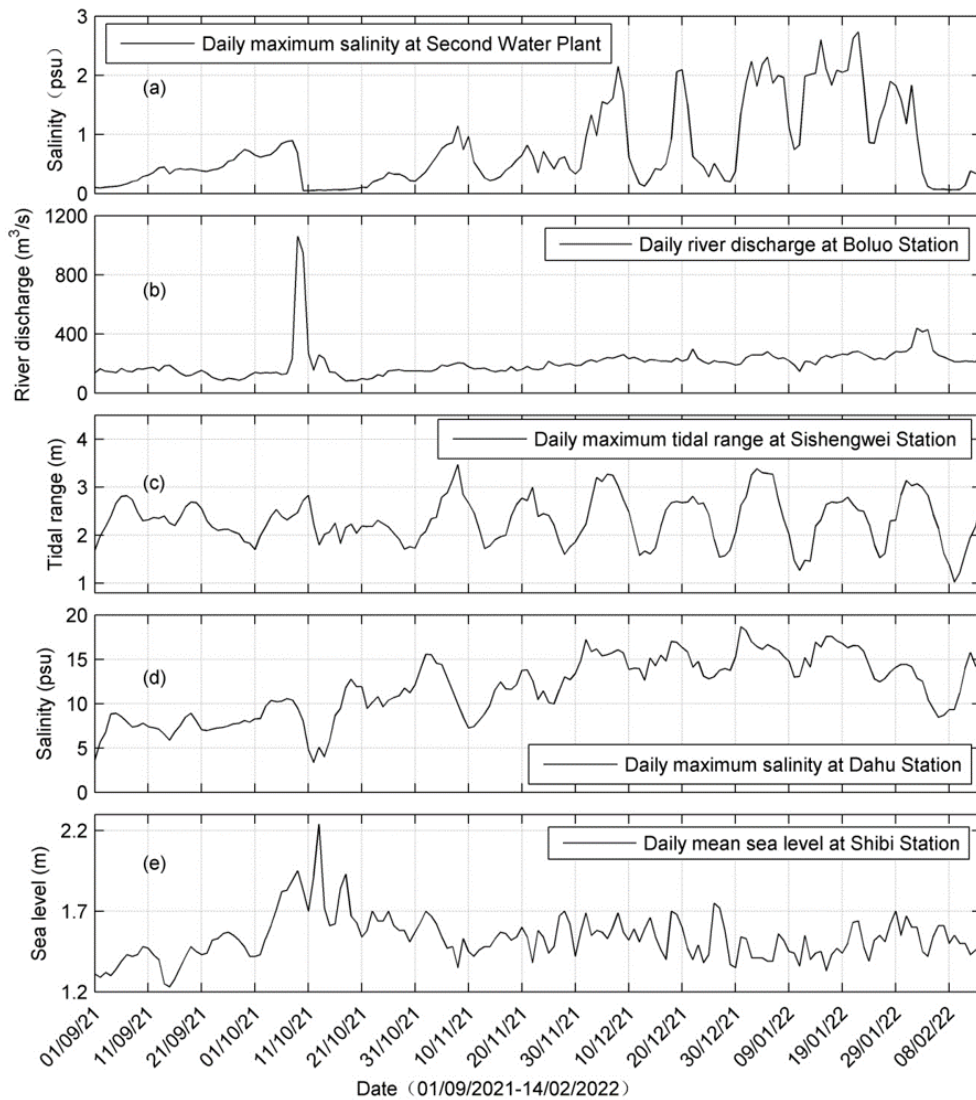tidal constituents of M_2, S_2, N2, K_1, O_1, as indicated by Payo-Payo et al. (2022).

Fig. 4 Wavelet analysis of the salinity at the Second Water Plant

To identify the possible factors influencing the salinity variations in the sub-

estuary, we present the time series data of salinity at the Second Water Plant, river

discharge at Boluo station, tidal range at Sishengwei station, salinity at Dahu station

(located in the main estuary), and daily sea level at Shibi station (located at the mouth of the main estuary) in Fig. 5. Firstly, it is evident that the variation of salinity at Dahu (Fig. 5d) shows a consistent pattern with the changes in tidal range at Sishengwei (Fig. 5c), when the river discharge is relatively low after a flash flood event, which occurred around October 21, 2021 (Fig. 5b). The highest salinity happened 2-3 days after neap tides in the transition from neap to spring tides, whereas the lowest salinity occurred in the transition from spring to neap tides, and generally occurred just before the neap tides. This result indicates that the salinity and tidal range in the main estuary were almost out of phase, and there existed a time lead of the salinity to the tidal range. This pattern agrees well with what occurred in the Hudson River (Bowen and Geyer, 2003) and the Modaomen Estuary (Gong and Shen, 2011), suggesting that the PRE remained in a state of partially mixed. On the other hand, the salinity of the Second Water Plant was almost in phase with the tidal range at the confluence (Fig. 5a vs. 5c). High salinities coincided with spring tides, and low salinities occurred during neap tides. It should be noted that the sea level at the PRE mouth showed a significant setup near October 11, 2021, when a large increase in river discharge was observed in the PRD due to a tropical storm (enumerated as the 17th typhoon in 2021, see the peak in Fig. 5b). This event caused a sharp decline in salinities at both Dahu and the Second Water Plant, followed by a rebound approximately 10 days later.

436

Fig. 5. Timeseries of: a) Daily maximum salinity at the Second Water Plant; b) Daily

discharge at Boluo station; c) Daily maximum tidal range at Sishengwei Station; d) Daily

maximum salinity at Dahu Station; e) Daily mean sea level at Shibi Station. Note that it takes

about 7-8 days after the storm for the salinity to recover to its pre-storm levels in the main estuary
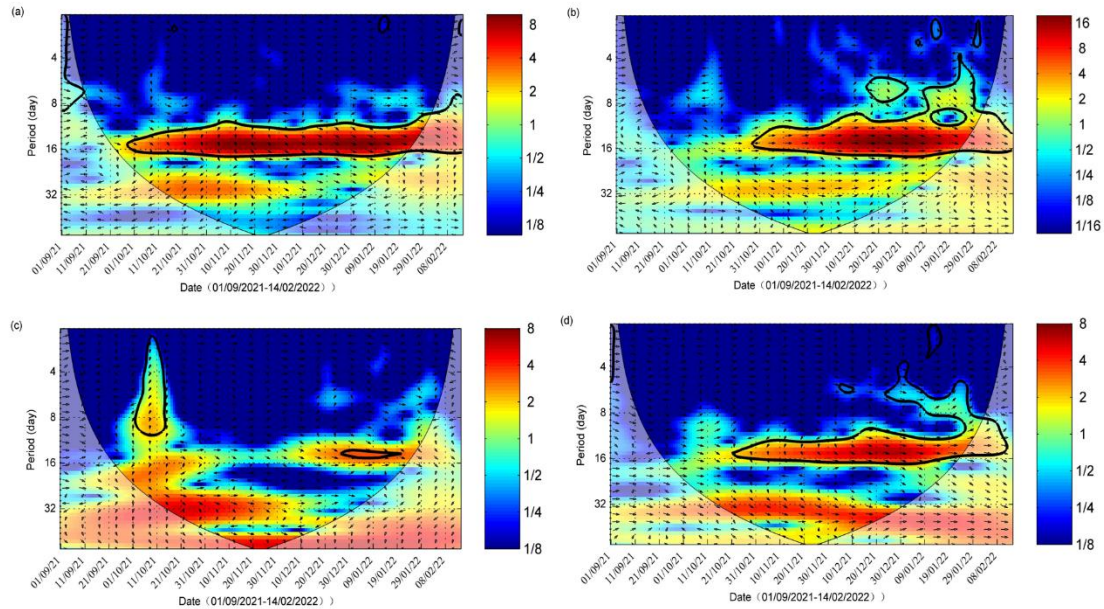
and almost a month in the sub-estuary

442

The cross-wavelet analysis between salinity at Dahu and tidal range at Sishengwei

(Figs. 6a) shows that the two variables are highly correlated in the periods of 14-16

days, indicating the effect of fortnightly spring-neap tidal variation. The arrow pointing

22

446 down and right in this time band demonstrates that the change in tidal range lagged the

447 variation of salinity.

448

Fig. 6. Cross-wavelet analysis of (a) between the salinity at Dahu and the tidal range at

Sishengwei; (b) between the salinity at the Second Water Plant and the tidal range at Sishengwei;

(c) between the salinity at the Second Water plant and the river discharge at the Boluo Station; (d)

between the salinity at the Second Water plant and that at the Dahu Station.

453

454 The cross-wavelet analysis between the salinity at the Second Water Plant and the

455 tidal range at Sishengwei station (Figs. 6b) shows that there existed a high common

456 power band of 14-16 days after October 21, 2021, and the phase relationship between

457 them was in phase, indicating that high salinities occurred during spring tides and low

458 salinities during neap tides, confirming the above results. It is also noted that before the

459 flood event on October 11, 2021, there was no high common power between these two

460 variables, even though the river discharge at the head of East River (Boluo Station) was

461   lower. This lack of high common power in the time band of 14-16 days before the

462   tropical storm event can also be noted in the cross-wavelet analysis between the salinity

463   at Dahu and the tidal range at Sishengwei. We also noted that before the storm event,

464   the water level at Sishengwei did not show distinct fortnightly spring-neap variations

465   (Fig. 5c). This lack of fortnightly cycle could be induced by the wind-induced

466   setup/setdown and/or the river-tide interaction, in which the river flow suppress the

467   tidal propagation. This phenomenon is peculiar and warrants a future study but beyond

468   the scope of this study.

469   The cross-wavelet analysis between the salinity at the Second Water Plant and the

470   river discharge at Boluo Station is presented in Fig. 6c. The high correlation during the

471   storm event was obvious, whereas, after that, the common power between the salinity

472   and river discharge was relatively low during the rebound period of the salinity at the

473   Second Water Plant. This low correlation could be due to the fact that the river discharge

474   did not change much and had no periodicity of 14-16 days then.

475   To examine the relationship between the salinities in the main estuary and at the

476   sub-estuary, we conducted a cross-wavelet analysis between the salinity at the Second

477   Water Plant and that at Dahu (Fig. 6d). There existed high common power between

478   these two variables in the time band of 14-16 days, the fortnightly tidal cycle. It also

479   shows that before October 21, 2021, the phase relationship between these two variables

480   was approximately in quadrature, indicating that the variation of the salinity at the

481   Second Water Plant lagged that at Dahu by 3.5-4 days. After October 21, 2021, the

482   phase relationship between them changed to in-phase when the river discharges in the

483 PRD became very low. This is quite interesting and will be explored in the following.
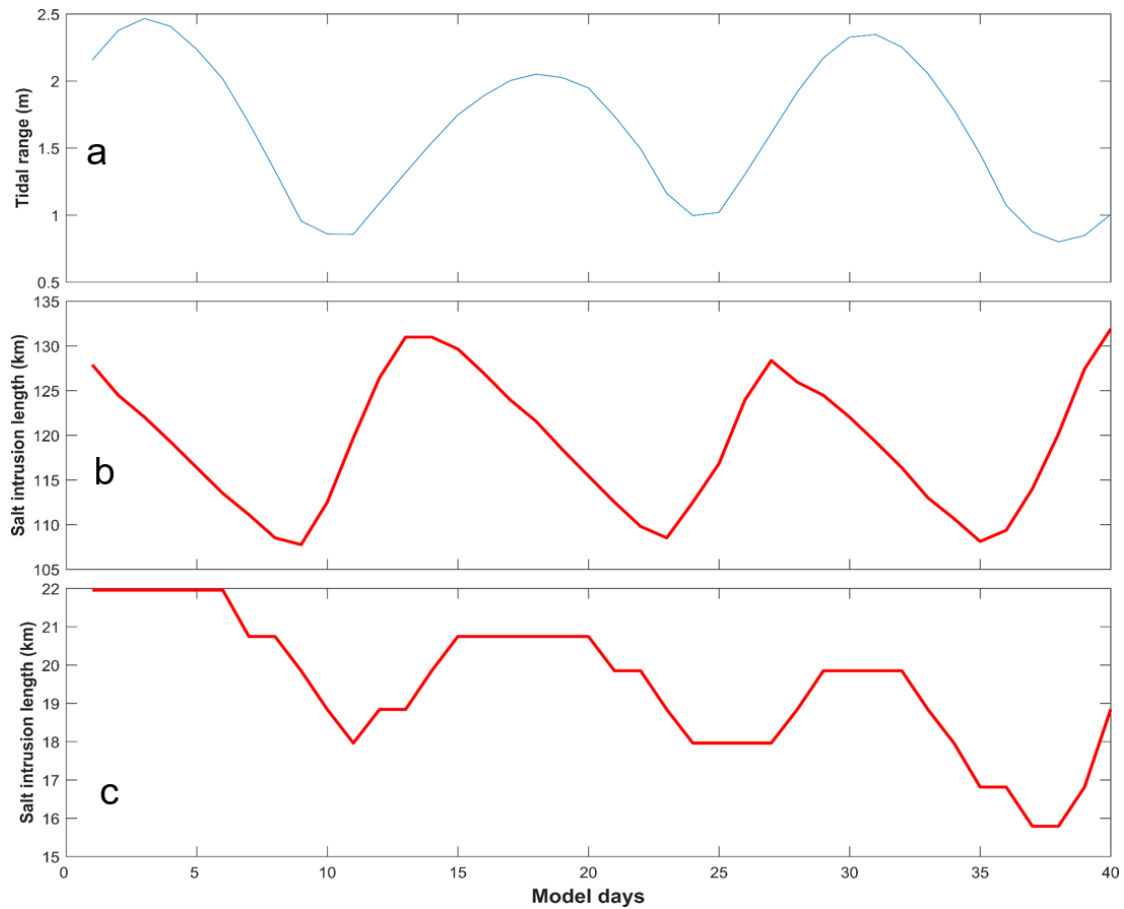
484

485 **4.2 The salt dynamics obtained through numerical simulations**

486

487 For Case 1 (base run), we intended to investigate the salt dynamics when the main

488 estuary stays in a state of partially mixed. Firstly we examine the variation of salt

489 intrusion length along the estuary's deep channel (Fig. 2b). Here the salt intrusion

490 length is defined as the distance of the bottom salinity isohaline of 5 ~~psu~~psu from the

491 estuary mouth. It shows that the tidal range at the main estuary's mouth fluctuates at

492 fortnightly and monthly timescales. There occur two spring –tides and neap tides in a

493 month (Fig. 7a), with one spring (neap) tide being stronger than the other one, as the

494 perigee/apogee cycle. The salt intrusion in the main estuary fluctuates with the tidal

495 range (Fig. 7b). The maximum salt intrusions occur just after neap tides, and the

496 minimum salt intrusions occur at the late of the transition from spring to neap tides,

497 consistent with the salinity change at the Dahu station shown above (Fig. 5d), and the

498 results we have demonstrated before (Gong et al., 2018). The relationship between the

499 salt intrusion and tidal range indicates an almost anti-phase one, suggesting that the

500 estuary is basically in a state of partially-mixed. This is because, for a partially-mixed

501 estuary, the landward salt transport is maximum during neap tides by the steady shear

502 and results in a maximum salt intrusion then. We present the tidally averaged

503 longitudinal profile of current and salinity for representative neap and spring tides in

504 Fig. S1 in the Supplement. The results confirm that during the neap tide, the estuary is

505 partially mixed, whereas, during the spring tide, the estuary becomes more mixed but

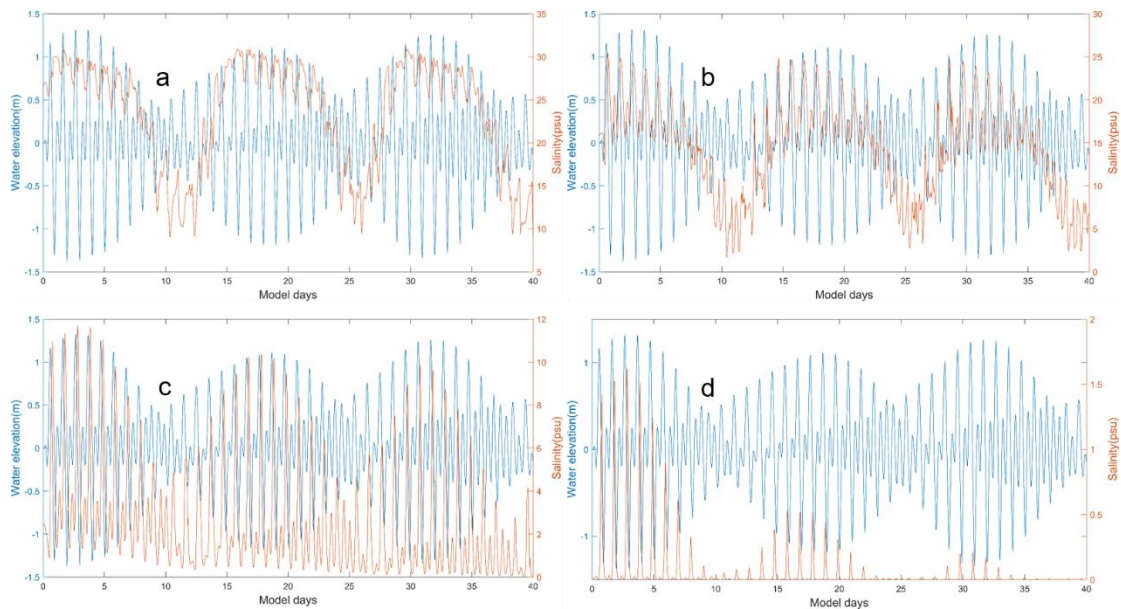506   still in the state of partially mixed.

508   Fig. 7. Timeseries of: a) tidal range at the mouth of the main estuary; b) salt intrusion length along

509   the longitudinal section of the main estuary; c) salt intrusion length along the longitudinal section

510   of the sub-estuary.

511

512   We also checked the time series data of surface salinity and water level at a station

513   (S1, Fig. 2b) in the main estuary, roughly corresponding to the Dahu Station (Fig. 8a).

514   It shows that the surface salinity increases from neap to spring tides, and reaches

515   maxima before spring tides. It declines from the maxima to minima from spring to neap

516   tides, reaching the minima almost at neap tides. This shows that the salinity increases

517   faster from neap to spring than decreases from spring to neap. This asymmetry is also

518 noted in the variation of salt intrusion length, which increases sharply after the neap

519 tides but decreases more gradually from the maximum to the minimum. This

520 phenomenon has been discussed by Chen (2015)–; when the salt intrusion length is

521 shorter just before the neap tide, the acceleration by the net landward salt flux is stronger,

522 whereas when the salt intrusion length is longer, the deceleration of salt intrusion length

523 by net seaward salt flux is relatively weaker. The change in salinity leads that in tidal

524 range during spring tides but lags the tidal range during neap tides.

526 Fig. 8. Timeseries of water level at the confluence and surface salinity a) at S1 Station in the main

527 estuary; b) at S2 station (the confluence); c) at S3 station in the middle of the sub-estuary; d) at S4

528 station in the upstream region of the sub-estuary.

529

530 Similar to the analysis of observation data, we then investigate the salt intrusion

531 in the sub-estuary (Fig. 7c). Though the accuracy is not high, as our model resolution

532 in the sub-estuary is not fine enough, it clearly shows that the maximum salt intrusions

533 occur nearly in spring tides and the minimum salt intrusions in neap tides. This means

that the salt intrusion is in phase with the tidal range in the sub-estuary. We show the tidally averaged profiles of current and salinity at the sub-estuary in Fig. S2 in the Supplement. It indicates that the sub-estuary is mostly in a state of well-mixed during both the neap and spring tides, though there appears some stratification near the mouth of the sub-estuary during the neap tide. The 1 ~~psu~~psu isohaline intrudes more in spring tides than in neap tides. It should be noted that at the lower reach of the sub-estuary, the surface salinity has a local high salinity zone (Fig. S2), consistent with the finding of Haywood et al. (1982) at the lower York River in the Chesapeake Bay, USA.

To examine the salinity variations along the sub-estuary, we selected three stations in the sub-estuary: one at the mouth (S2), one in the middle reach (S3), and the last one in the upper reach (S4). The time series of water level at the confluence and salinities at these three stations are shown in Figs. 8b, 8c and 8d. The salinity at the mouth of the sub-estuary (Fig. 8b) fluctuates similarly to that in the main estuary: maximum salinities occur right after neap tides and minimum salinities just before neap tides. In the middle of the sub-estuary (Fig. 8c), the salinity variation almost keeps pace with that of the tidal range: maximum salinities occur at spring tides and minimum salinities at neap tides. At the upstream station, the salinity variation shows a similar pattern to that in the middle of the sub-estuary. This indicates that when saline water propagates upstream, it advances more landward and experiences less impedance during spring tides and vice versa. We explore this phenomenon in the discussion part.

4.3 The subtidal salt dynamics in the sub-estuary by the analytical solution
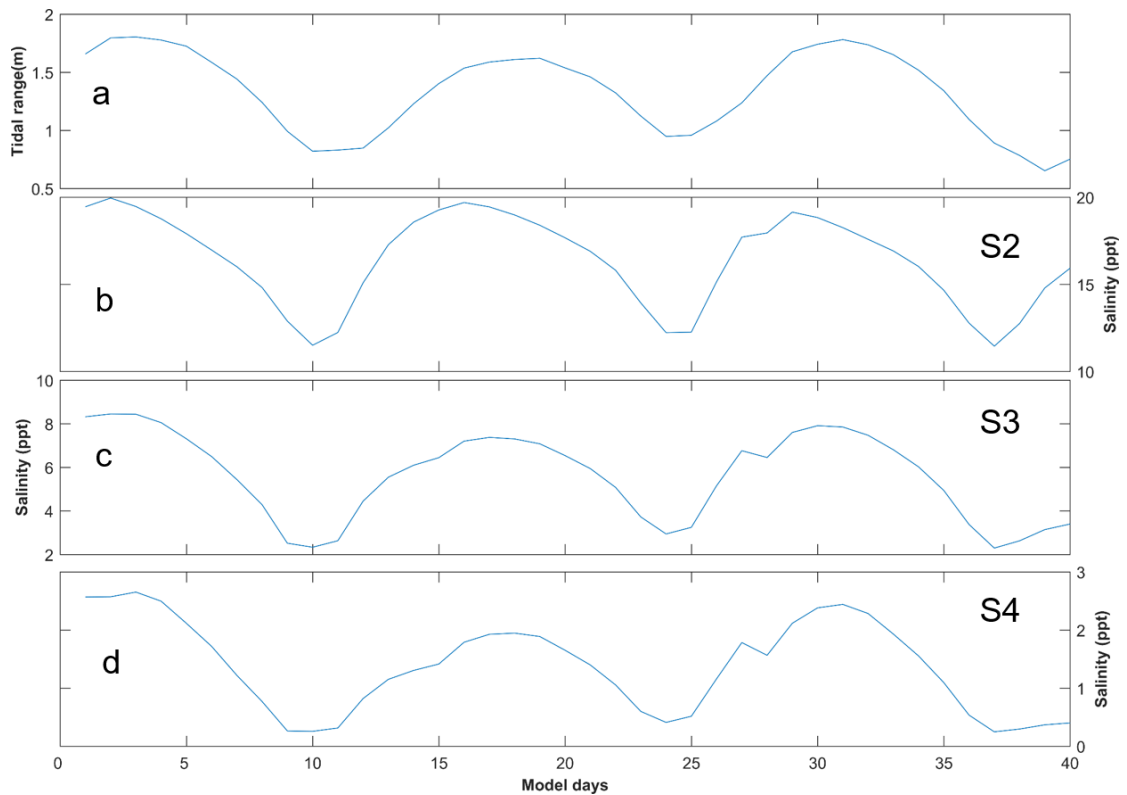
557   We used the analytical solutions in Section 3.3 to explore the salt dynamics in the

558   sub-estuary. In the sub-estuary, the exponential decaying constant of the cross-sectional

559   area was calculated to be 50 km; and the river discharge was specified to be 200 m³ s⁻

560   ¹.

561   We used the scheme of constant dispersion along the sub-estuary, and the K_x was

562   estimated as (Ralston et al., 2008):

$$K_x = c_h(\frac{T_{tide}}{4}U_T)U_T \qquad (89)$$

564   where c_h is an empirical constant of 0.0224, T_{tide} is the tidal period, here is set as

565   12.42 hours; U_T is the tidal current amplitude at the sub-estuary's mouth.

566   We solved Eq. (56) for the model experiment Case 1. The results are shown in Fig.

567   9.

569   Fig. 9. The results of the analytical solution of salinity variations along the sub-estuary. a)

570   tidal range at the mouth of the sub-estuary; b), c), and d) are subtidal salinity variations at S2,

29

571   S3, and S4 stations.

572

573   Under the 1500 m^3 s^{-1} river discharge at the head of the main estuary, the tidal

574   range at the sub-estuary's mouth varies between spring and neap tides, with a greater

575   spring and a weaker spring in a month (Fig. 9a). The subtidal salinity at the confluence

576   (S2 station, Fig. 9b) varies between 10 and 20 ~~psu~~psu, with the maximum salinities

577   occurring before the spring tides and the minimum salinities before the neap tides,

578   indicating a phase lead of salinity to the tidal range. In the middle of the sub-estuary

579   (S3 station, Fig. 9c), the salinity fluctuates between 2 and 10 ~~psu~~psu, and there exists a

580   slight phase lead of salinity to that of the tidal range. In the upstream region of the sub-

581   estuary (S4 station, Fig. 9d), the salinity fluctuates between 0 and 3 ~~psu~~psu, and the

582   salinity variation becomes almost in phase with that of the tidal range at the confluence.

583   Compared to the numerical simulation results, the analytical solution reproduces the

584   trend of the phase relationship between the salinity and tidal range along the sub-estuary:

585   the phase of the salinity variation leads that of the tidal range at the sub-estuary's mouth

586   and becomes more in phase with that of the tidal range in the middle and upstream

587   region of the sub-estuary. Meanwhile, the fluctuation magnitude in the middle of the

588   sub-estuary is well reproduced. However, the fluctuation range in the upstream region

589   of the sub-estuary is over-estimated, showing the weakness of assuming a uniform

590   horizontal dispersion along the sub-estuary.

591

592   **5. Discussion**
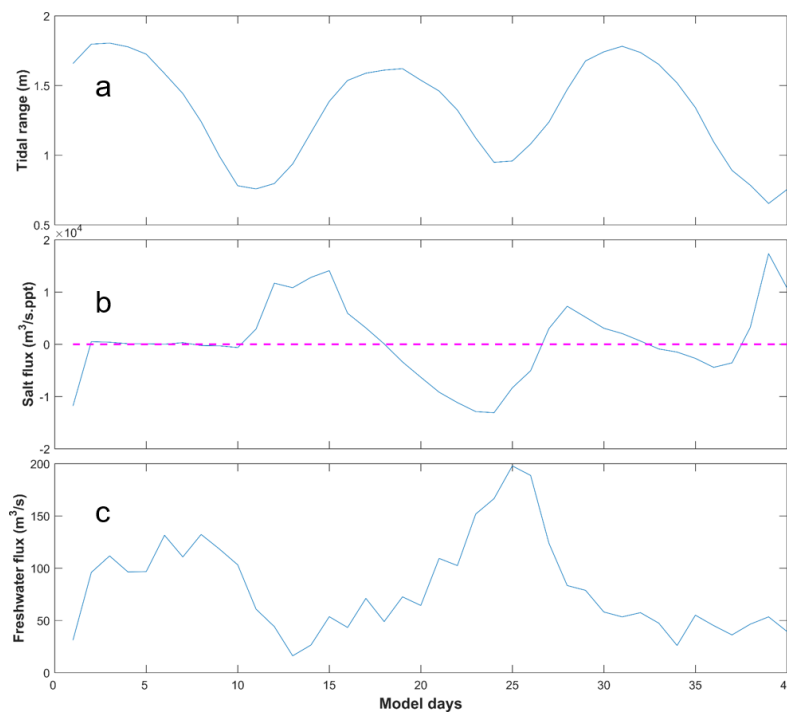
593

594   **5.1 The physics behind the change in phase relationship between the salinity and**

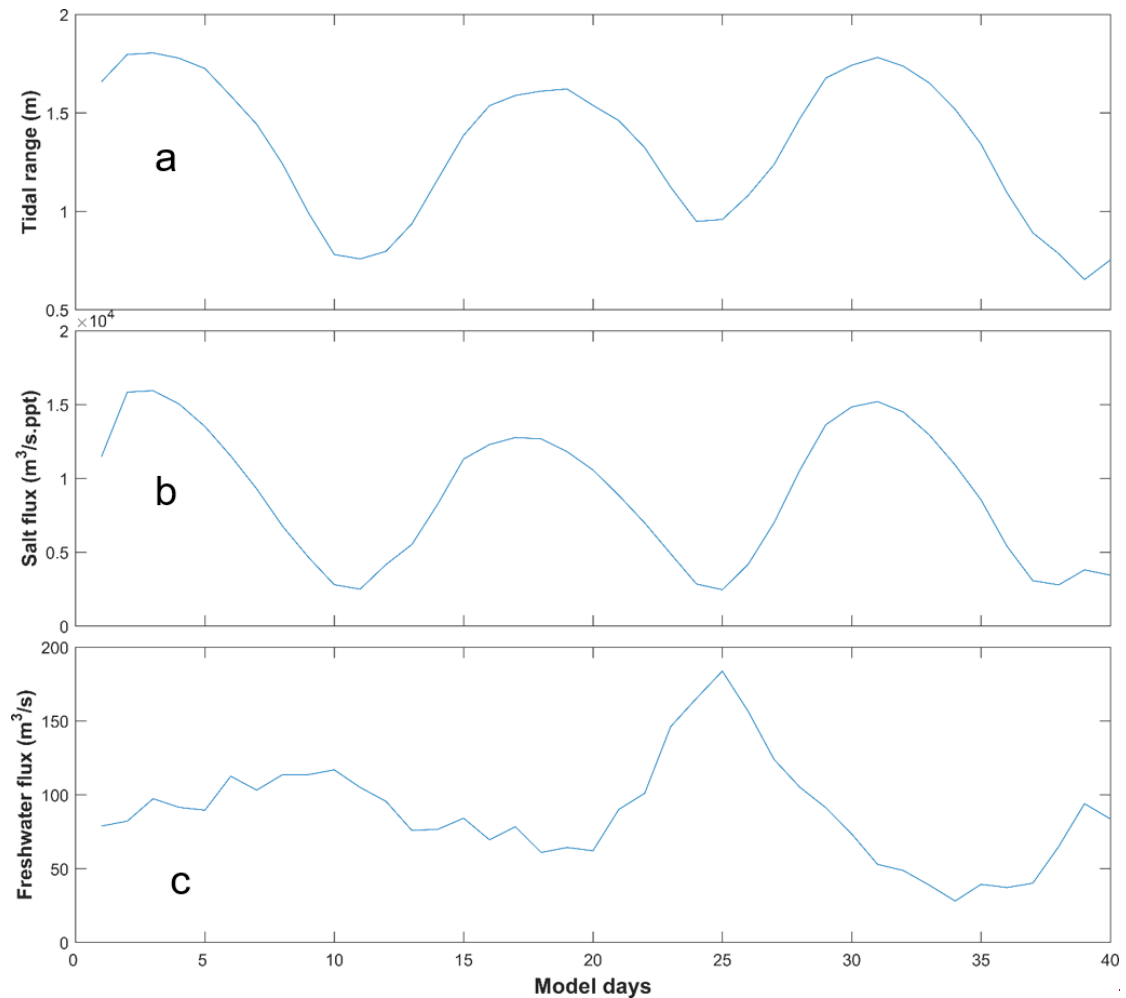595   **tidal range along the sub-estuary**

596

597   The numerical results and analytical solutions both indicate that near the sub-

598   estuary's mouth, the salinity fluctuation leads that of the tidal range, and in the middle

599 and upstream region of the sub-estaury, the salinity variation becomes more in phase

600 with that of the tidal range. The analytical solution shows that the changes in the phase

601 relationship between these two variables are mostly caused by the change in horizontal

602 dispersion, that is, the larger dispersions during spring tides cause increased landward

603 salt transport, resulting in elevated salinity in the middle and upstream regions of the

604 sub-estuary. The results of numerical simulation are a combination of many

605 interweaved processes and a little harder to interpret. To unravel the physics in the

606 numerical simulation, we examine the salt transport in the lower reach at a cross-section

607 near the sub-estuary mouth and freshwater transport in the upstream cross-section of

608 the sub-estuary (shown in Fig. 2b).

609

Fig. 10. Timeseries of: a) tidal range at the mouth of the sub-estuary; b) salt flux at the cross-section near the mouth of the sub-estuary; c) freshwater flux at the cross-section in the upstream region of the sub-estuary. It should be noted that the freshwater flux is the magnitude and has a sign opposite to the salt flux.

The results are shown in Fig. 10. From Fig. 10b, the subtidal salt flux near the sub-estuary's mouth is ~~always~~ generally landward during the periods from neap tides to spring tides and seaward from spring tides to neap tides~~in the simulation period and is higher during spring tides and lower during neap tides~~. The change in salt flux leads

that of the tidal range, consistent with the phase relationship between salinity and tidal

range near the sub-estuary's mouth (Fig. 8b). As the sub-estuary is well-mixed during

the simulation period, the landward salt transport is mostly induced by the tidal

oscillatory transport ~~and justifies ignoring the steady shear part in Eq. (3)~~. The subtidal

freshwater flux in the upstream region of the sub-estuary is seaward, and shows a

pattern that larger freshwater fluxes occur during neap tides and smaller freshwater

fluxes during spring tides (Fig. 10c). This pattern has been well studied by Buschman

et al. (2009) in the subtidal momentum dynamics. They showed that the primary

subtidal momentum balance is between the water level gradient and bottom friction.

During spring tides, the subtidal bottom friction is larger and the subtidal water slope

is greater, meaning that more freshwater is being detained upstream to elevate the water

level there. During neap tides, the detained freshwater in the upstream is released

downstream and results in increased freshwater fluxes. In this way, the saline water

from the sub-estuary's mouth experiences less impedance and dilution during spring

tides and thus advances more landward, resulting in an enhanced salt intrusion during

spring tides, and vice versa. The above results indicate that the more in-phase

relationship between the salinity and tidal range in the middle and upstream region of

the sub-estuary is mostly generated by the fortnightly variation of the tidal strength and

the associated variations of horizontal dispersion and freshwater flux by the river-tide

interaction. The larger the dispersion, the more salt is pumped into the upstream. The

stronger the tidal strength, the more freshwater is detained upstream and less impedance
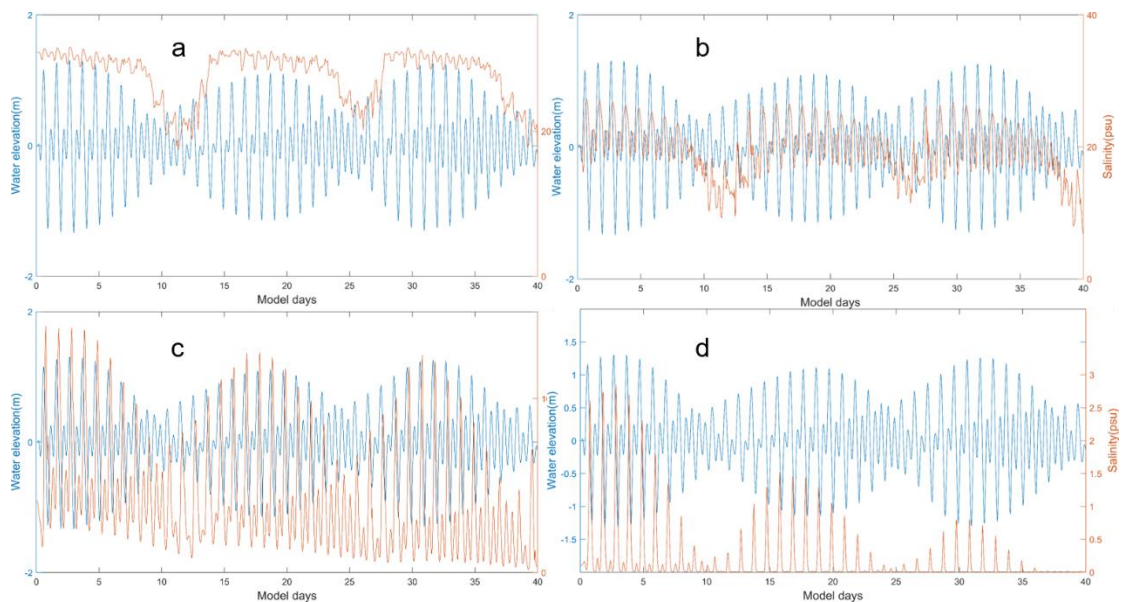
to the salt intrusion.

643   From the above results, it is seen that the salinity dynamics in the sub-estuary show

644   a pattern that is more influenced by the main estuary in the lower reach and becomes

645   more controlled by internal tidal processes in the middle and upstream regions of the

646   sub-estuary.

647

648   **5.2 How do the salt dynamics in the main estuary affect that in the sub-estuary?**
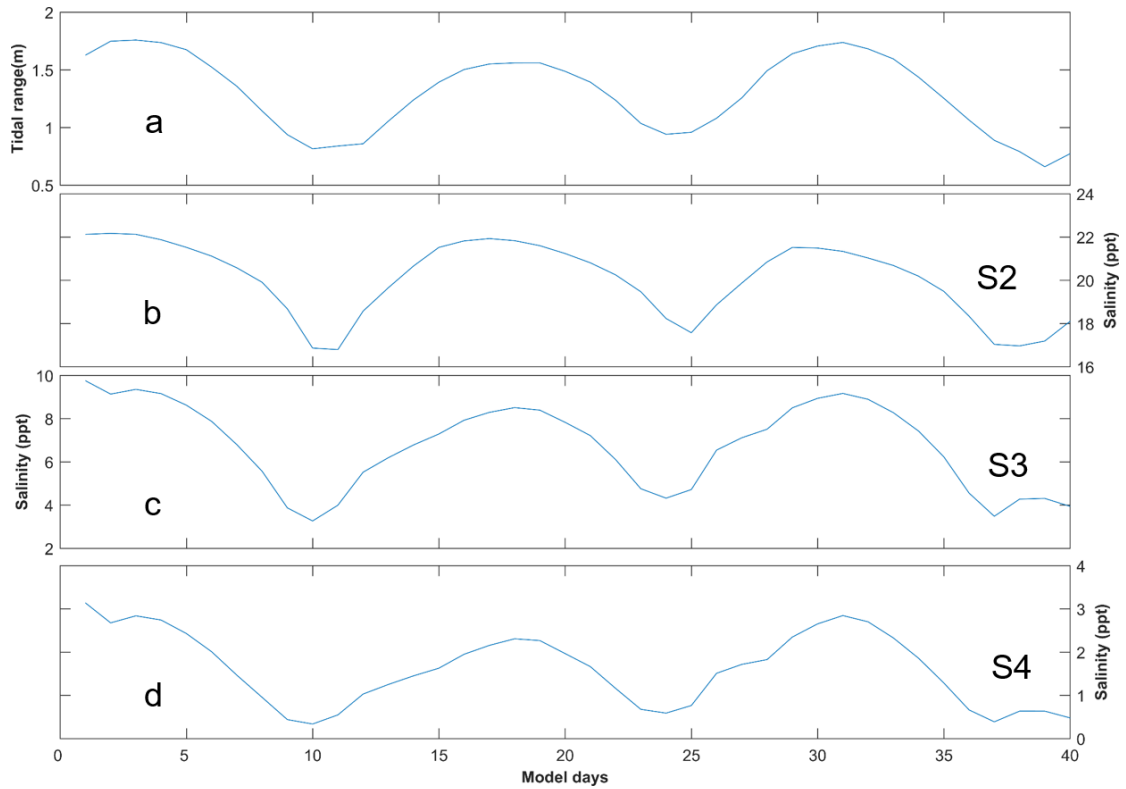
649

650   To further study how the changes in salinity dynamics in the main estuary affect

651   the salinity variation in the sub-estuary, we set up another experiment. In the model

652   scenario of Case 2, we set an extremely low river discharge (500 m^3 s^{-1}) at the head of

653   the main estuary, and the results are shown in Fig. 11. Simultaneously, the analytical

654   solutions for the scenario of Case 2 are presented in Fig. 12.

655

656   Fig. 11. Timeseries of water level at the confluence and surface salinity under the

657   extremely lower river discharge in the main estuary at stations of: a) S1; b) S2; c) S3; d) S4.

658

Fig. 12. The results of the analytical solution of salinity variations along the sub-estuary under extremely dry conditions. a) tidal range at the mouth of the sub-estuary; b), c), and d) are subtidal salinity variations at S2, S3, and S4 stations.

With decreased river discharge from the head of the main estuary, the salt intrusion front is shifted more landward. The S1 station is now located in the polyhaline region with a mean salinity of approximately 26 ~~psu~~psu (Fig. 11a). The minimum salinities coincide more with neap tides but the maximum salinities occur around spring tides. The asymmetry between salinity rise and fall is decreased, with salinities jumping quickly after neap tides, keeping elevated around spring tides, and dropping quickly just before neap tides. For the intratidal variation, it can be seen that during a tidal cycle, the salinity fluctuation is reduced when compared to Case 1 (Figs. 11a vs 8a), which is mostly due to the fact that with the reduced river discharge, the salinity gradient in the

35

673   polyhaline reach of the main estuary is decreased.

674   For the S2 Station (at the confluence, Figs. 11b and 12b), it is now located in the

675   mesohaline region, with the salinity ranging from 5 to 26 ~~psu~~psu. The highest and

676   lowest salinities are both increased when compared to Case 1, with a reduced magnitude

677   of salinity change in a tidal cycle. The salinity variation pattern remains similar to that

678   in Case 1, with minimum salinities occurring just before neap tides, and maximum

679   salinities after neap tides, but occur closer to spring tides. The asymmetry of quick

680   increase from neap to spring but gradual decrease afterwards is still clear.

681   When entering into the sub-estuary, the salinity variation at S3 in the middle of the

682   sub-estuary shows a more in-phase relationship between salinity and tidal range (Figs.

683   11c and 12c). The maximum salinities occur closer to spring tides whereas the

684   minimum salinities still occur just before neap tides. In the upstream region of the sub-

685   estuary (Figs. 11d and 12d), the phase relationship between salinity and tidal range is

686   also an in-phase one. Combined with the situation at the S1 Station, it indicates that the

687   variations of salinity at stations S4 and S1 are more synchronous. This largely explains

688   the observed phenomenon that under more drought conditions, the salinity variations at

689   the Second Water Plant kept pace with those at the Dahu Station (Section 3.1).

690

691   **5.3 Limitations and implications of this study**

692

693   In this study, we focus on the phase relationship between the variations of salinity

694   and tidal range, both in a sub-estuary and the main estuary. The salinity variations along

695   the sub-estuary are revealed to be associated with the salinity dynamics in the main

estuary, linked by the salinity variations at the confluence between the main estuary and the sub-estuary. In a spring-neap tidal cycle, even when the salinity at the confluence is a little lower during the spring tide than that during the neap tide, the higher horizontal dispersion and decreased freshwater release at the head of the sub-estuary during the spring tide can pump more saline water from the confluence into the middle and upstream of the sub-estuary, and cause the salinities there to be higher than during the neap tide. In this way, the salinity variations at areas farther away from the confluence become more synchronous with the tidal range.

However, this study did not consider the effect of winds and waves, as shown to be important in previous studies such as Gong et al. (2018). The variations of salinity in the period of 5-8 days should be related to the wind effects and await future exploration. The effect of sea level change outside the main estuary was also not examined in detail, though it can be intrinsically linked to the effect of winds and waves. Finally, we did not explore a full parameter space of river discharge, tidal range, and bathymetry situations, and thus can not give a synthesis of the sub-estuary salt intrusion dynamics at this time.

Despite all these limitations, this study has implications for studying salt intrusion dynamics in sub-estuaries, which are influenced by both the hydrodynamics inside the sub-estuary and the salt dynamics in the main estuaries. It is also of importance for providing a scientific basis for salt intrusion mitigation in the region. For example, salt intrusion in the sub-estuary is not only impacted by the river discharge from the head of the sub-estuary itself but also largely affected by the salt dynamics in the main estuary.

718   In this respect, apart from releasing more freshwater from the upstream in the sub-

719   estuary, measures to control the salinity variations at the confluence between the main

720   estuary and the sub-estuary also need to be taken into consideration. This may involve

721   implementing engineering solutions such as the construction of barriers or gates to

722   regulate the inflow of saltwater from the main estuary into the sub-estuary. Additionally,

723   the management of water withdrawals and releases in the sub-estuary and main estuary

724   needs to be optimized by taking the estuarine system as a whole. Overall, a

725   comprehensive and coordinated approach is necessary to effectively mitigate salt

726   intrusion in sub-estuaries.

727

728   **6. Summary and conclusions**

729

730   From 2021 to 2022, under the influence of an extended La Nina event, the Pearl

731   River Delta region in China experienced a prolonged extreme drought condition, and

732   the sub-estuary (East River estuary) also suffered greatly from the enhanced salt

733   intrusion. To identify the characteristics of the salt intrusion in the sub-estuary, and to

734   explore the underlying physics in controlling the spatio-temporal variations of the salt

735   intrusion, we collected observation data and conducted numerical simulations for

736   idealized estuarine bathymetry, and used analytical solutions for the subtidal salinity

737   variations in the sub-estuary. The observation data showed that the salinity variation in

738   the main estuary usually led that of the tidal range, and the asymmetry between salinity

739   rise and fall in a fortnightly timescale was prominent. However, in the upstream region

740   of the sub-estuary, the salinity variation was in phase with that of the tidal range, and

741 the salinity rise and fall were more symmetrical. The idealized model simulations and

742 the analytical solution both reproduced these phenomena.

743 We note that under drought conditions, the river-tide interaction played a role in

744 the in-phase relationship between the salinity and tidal range upstream region of the

745 sub-estuary. The salinity variation in the middle and upstream regions of the sub-

746 estuary can keep pace with that of the tidal range. The analytical results show that the

747 horizontal dispersion scaling with tidal strength can largely reproduce the changes in

748 phase relationship between salinity and tidal range in the sub-estuary. We conclude that

749 both the changes in horizontal dispersion and the river-tide interaction in modulating

750 the freshwater release are responsible for the in-phase relationship between the salinity

751 and tidal range in the middle and upstream regions of the sub-estuary.

752 This study is of help in the investigation of salt dynamics in sub-estuaries

753 connected to main estuaries, and of implications for mitigating salt intrusion problems

754 in the regions suffered from enhanced salt intrusion by climate change and human

755 interventions.

756

757 **Data availability:** The observation data can be downloaded from the website

758 http://www.pearlwater.gov.cn/. The numerical data is available upon request to the

759 corresponding author.

760

761 **Declaration of competing interest**

The contact author has declared that none of the authors has any competing

interests.

CRediT authorship contribution statement

Zhongyuan Lin: Data collection, wavelet analysis, Writing - original draft, Writing -

review & editing. **Guang Zhang:** numerical modeling, Writing - review & editing.

Huazhi Zou: Writing-review &editing, funding acquisition. **Wenping Gong**:

Conceptualization, Methodology, Writing-review &editing, funding acquisition.

Supplement:

We present the longitudinal profiles of subtidal current and salinity along the

channels in the main estuary and the sub-estuary during typical spring and neap tides.

Fig. S1 is for the dry condition with 1500 m^3/s at the head of the main estuary, and Fig.

S2 for the extremely dry condition with 500 m^3/s released at the head of the main estuary.

References

Bowden, K. F., 1965. Horizontal mixing in the sea due to a shearing current. Journal of

787   Fluid Mechanics 21, 83-95. https://doi.org/10.1007/BF00167972

788 Bowen, M., Geyer, W.R., 2003. Salt transport and the time-dependent salt balance of a

789   partially stratified estuary. Journal of Geophysical Research 108(C5), 3185.

790   Doi:10.1029/2001JC001231.

791 Buschman, F. A., Hoitink, A. J. F., Vegt., M. V. D., 2009. Subtidal water level variation

792   controlled by river flow and tides. Water Resources Research 45(10), W10420.

793   https://doi.org/10.1029/2009WR008167

794 Cai, H., Savenije, H.H.G., Zuo, S., Jiang, C., Chua, V.P., 2015. A predictive model for

795   salt intrusion in estuaries applied to the Yangtze estuary. Journal of Hydrology 529,

796   1336-1349.

797 Chapman, D. C., 1985. Numerical Treatment of Cross-Shelf Open Boundaries in a

798   Barotropic Coastal Ocean Model. Journal of Physical Oceanography 15(8), 1060-

799   1075.

800 Chen S.-N., 2015. Asymmetric Estuarine Responses to Changes in River Forcing: A

801   Consequence of Nonlinear Salt Flux. Journal of Physical Oceanography 45(11),

802   2836-2847. https://doi.org/10.1175/JPO-D-15-0085.1

803 Dong, L., Su, J., Wong, L., Cao, Z., Chen, J.-C., 2004. Seasonal variation and dynamics

804   of the Pearl River plume. Continental Shelf Research 24(16), 1761-1777.

805   https://doi.org/10.1016/j.csr.2004.06.006

806 Flather, R. A., 1976. A tidal model of the northwest European continental shelf, A tidal

807   model of the northwest European continental shelf. Mem. Soc. R. Sci. Liege 10(6),

808   141-164.

809   Gong, W., Shen, J., 2011. The response of salt intrusion to changes in river discharge

810   and tidal mixing during the dry season in the Modaomen Estuary, China.

811   Continental Shelf Research, 31, 769–788.

812   Gong, W., Lin, Z., Chen, Y., Chen, Z., Zhang, H., 2018. Effect of winds and waves on

813   salt intrusion in the Pearl River estuary. Ocean Science 14(1), 139-159.

814   https://doi.org/10.5194/os-14-139-2018

815   Gong, W., Chen, L., Zhang, H., Yuan, L., Chen, Z., 2020. Plume Dynamics of a Lateral

816   River Tributary Influenced by River Discharge From the Estuary Head. Journal of

817   Geophysical Research: Oceans. doi: 10.1029/2019JC015580.

818   Gong, W., Lin, Z., Zhang, H., Lin H., 2022. The response of salt intrusion to changes

819   in river discharge, tidal range, and winds, based on wavelet analysis in the

820   Modaomen estuary, China.Ocean & Coastal Management 219, 106060.

821   https://doi.org/10.1016/j.ocecoaman.2022.106060

822   Haidvogel, D. B., Arango, H. G., Hedstrom, K., Beckmann, A,.Malanotte-Rizzoli, B.,

823   Shchepetkin, A., F., 2000. Model evaluation experiments in the North Atlantic

824   Basin: Simulations in nonlinear terrain-following coordinates. Dynamics of

825   Atmospheres and Oceans 32(3-4), 239-281.https://doi.org/10.1016/S0377-

826   0265(00)00049-X

827   Haywood, D., Welch, C. S., Hass, L. W., 1982. York River destratification: an estuary-

828   sub-estuary interaction. Science 216, 1413-1414.

829   https://doi.org/10.1126/science.216.4553.1413

830   Hong, B., Liu, Z., Shen, J., Wu, H., Gong, W., Xu, H., Wang, D., 2020. Potential

831   physical impacts of sea-level rise on the Pearl River Estuary, China. Journal of

832   Marine Systems201, 103245. https://doi.org/10.1016/j.jmarsys.2019.103245

833   Hu, J., Li, S., Geng, B., 2011. Modeling the mass flux budgets of water and suspended

834   sediments for the river network and estuary in the Pearl River Delta, China. Journal

835   of Marine Systems 88(2), 252-266. https://doi.org/10.1016/j.jmarsys.2011.05.002

836   Jia, L., Luo, Z., Yang, Q., Ou, S., Lei, Y., 2006. The impact of massive sand mining on

837   the morphology and tidal dynamics in the downstream of East River and the East

838   River Delta (In Chinese). Acta Geographica Sinica 2006(09), 985-994.

839   Liu, B., Yan, S., Chen, X., Lian, Y., Xin, Y., 2014. Wavelet analysis of the dynamic

840   characteristics of saltwater intrusion - A case study in the Pearl River Estuary of

841   China. Ocean & Coastal Management 95, 81-92.

842   https://doi.org/10.1016/j.ocecoaman.2014.03.027

843   MacCready, P., Geyer, W. R., 2010. Advances in estuarine physics. Annual Review of

844   Marine Science 2(1), 35–58. https://doi.org/10.1146/annurev-marine-120308-

845   081015.

846   Mao, Q., Shi, P., Yin, K., Gan, J., Qi, Y., 2004. Tides and tidal currents in the Pearl River

847   Estuary. Continental Shelf Research 24(16), 1797-1808.

848   https://doi.org/10.1016/j.csr.2004.06.008

849   Okubo, A., 1973. Effect of shoreline irregularities on streamwise dispersion in estuaries

850   and other embayments. Netherlands Journal of Sea Research 6, 213-224.

851   https://doi.org/10.1016/0077-7579(73)90014-8

852   Orlanski, I., 1976. A simple boundary condition for unbounded hyperbolic flows.

Journal of Computational Physics 21(3), 251–269. http://dx.doi.org/10.1016/0021-9991(76)90023-1

Payo-Payo, M., Bricheno, L. M., Dijkstra, Y. M., Cheng, W., Gong, W., Amoudry, L. O., 2022. Multiscale temporal response of salt intrusion to transient river and ocean forcing. Journal of Geophysical Research: Oceans *127*, e2021JC017523. https://doi. org/10.1029/2021JC017523.

Ralston, D. K., Geyer, W. R., Lerczak J. A., 2010. Structure, variability, and salt flux in a strongly forced salt wedge estuary, J. Geophys. Res., 115, C06005, doi:10.1029/2009JC005806.

Ralston, D. K., Geyer, W. R., 2019. Response to channel deepening of the salinity intrusion, estuarine circulation, and stratification in an urbanized estuary. Journal of Geophysical Research: Oceans 124, 4784–4802. https://doi.org/10.1029/2019JC015006

Savenije, H.H.G., 2012. Salinity and tides in alluvial estuaries. Second Edition <www.salinityandtides.com>.

Shchepetkin, A. F., McWilliams, J. C., 2005. The regional ocean modeling system (ROMS): A split-explicit, free-surface, topography-following coordinates oceanic model. Ocean Modeling 9, 347–404.

Simpson, J.H., Brown, J., Matthews, J.P., Allen, G., 1990. Tidal straining, density currents, and stirring in the control of estuarine stratification. Estuaries 13 (2), 125–132.

Smagorinsky, J., 1963. General Circulation Experiments with the Primitive Equation,

Part 1, the Basic Experiment. Monthly Weather Review 91(3), 99-164. http://dx.doi.org/10.1175/1520-0493

Spinoni, J., Naumann, G., Carrao, H., Barbosa, P., Vogt, J., 2014. World drought frequency, duration, and severity for 1951–2010. Int. J. Climatol. 34, 2792–2804.

Stommel, H., Farmer, H. G., 1952. On the nature of estuarine circulation: part I (chapters 3 and 4). Woods Hole Oceanographic Institution.

Umlauf, L., Burchard, H., 2003. A generic length-scale equation for geophysical turbulence models. Journal of Marine Research 61(2), 235-365. https://doi.org/10.1357/002224003322005087

Uncles, R. J., Stephens, J. A., 2010. Turbidity and sediment transport in a muddy sub-estuary. Estuarine, Coastal and Shelf Science 87(2), 213-224. https://doi.org/10.1016/j.ecss.2009.03.041

Warner, J. C., Sherwood, C. R., Arango, H. G., Signell, R. P., Butman, B., 2005. Performance of four turbulence closure models implemented using a generic length scale method. Ocean Modeling8, 81–113.

Wei, X., Kumar, M., Schuttelaars, H.M., 2017. Three-dimensional salt dynamics in well-mixed estuaries: influence of estuarine convergence, Coriolis, and bathymetry. Journal of Physical Oceanography 47, 1843-1872.

Wong, L. A., Chen, J. C., Xue, H., Dong, L. X., Su, J. L., Heinke, G., 2003. A model study of the circulation in the Pearl River Estuary (PRE) and its adjacent coastal waters: 1. Simulations and comparison with observations. Journal of Geophysical

896   Research 108(C5). https://doi.org/10.1029/2002jc001451

897   Wu, Z. Y., Saito, Y., Zhao, D. N., Zhou, J. Q., Cao, Z. Y., Li, S. J., 2016. Impact of

898   human activities on subaqueous topographic change in Lingding Bay of the Pearl

899   River estuary, China, during 1955-2013. Scientific Reports 6, 37742.

900   https://doi.org/10.1038/srep37742

901   Yellen, B., Woodruff, J. D., Ralston, D. K., MacDonald, D. G., Jones. D. S., 2017. Salt

902   wedge dynamics lead to enhanced sediment trapping within side embayments in

903   high-energy estuaries. Journal of Geophysical Research: Oceans 122(3), 2226-

904   2242. https://doi.org/10.1002/2016JC012595

905   Zhang, P., Yang, Q., Wang, H., Cai, H., Liu, F., Zhao, T., Jia, L., 2021. Stepwise

906   alterations in tidal hydrodynamics in a highly human-modified estuary: The roles

907   of channel deepening and narrowing. Journal of Hydrology 597, 126153.

908   Zimmerman, J. T. F., 1986. The tidal whirlpool: A review of horizontal dispersion by

909   tidal and residual currents. Netherlands Journal of Sea Research 20, 133-154.

910   https://doi.org/10.1016/0077-7579(86)90037-2

911

912

Figure Captions:

914

Fig.1. a) The East River estuary; b) Map of the Pearl River Delta and the locations of hydrological and water level stations.

Fig. 2. Geometry and bathymetry of the idealized model domain: a)for the whole domain; b)zoom in for the area of concern. The origin of the coordinates is in the middle of the main estuary mouth. The longitudinal sections in the main and sub-estuary are shown as dashed lines, and the cross-sections inside the sub-estuary are shown as color solid lines. The locations of several stations are indicated.

Fig.3. Timeseries of: a) Daily maximum salinity at the Second Water Plant; b) Total duration period with salinity exceeding 0.5 ~~psu~~psu for each month; c) Monthly river discharge at Boluo station (upstream of the East River); d) Monthly river discharge at Wuzhou station (upstream of the West River); e) Monthly river discharge at Shijiao station (upstream of the North River).

Fig. 4 Wavelet analysis of the salinity at the Second Water Plant.

Fig. 5. Timeseries of: a) Daily maximum salinity at the Second Water Plant; b) Daily river discharge at Boluo station; c) Daily maximum tidal range at Sishengwei Station; d) Daily maximum salinity at Dahu Station; e) Daily mean sea level at Shibi Station.

Fig. 6. Cross-wavelet analysis of (a) between the salinity at Dahu and the tidal range at Sishengwei; (b) between the salinity at the Second Water Plant and the tidal range at Sishengwei; (c) between the salinity at the Second Water plant and the river

935   discharge at the Boluo Station; (d) between the salinity at the Second Water plant and

936   that at the Dahu Station.

937   Fig. 7. Timeseries of: a) tidal range at the mouth of the main estuary; b) salt

938   intrusion length along the longitudinal section of the main estuary; c)salt intrusion

939   length along the longitudinal section of the sub-estuary.

940   Fig. 8. Timeseries of water level at the confluence and surface salinity a) at S1

941   Station in the main estuary; b) at S2 station (the confluence); c) at S3 station in the

942   middle of the sub-estuary; d) at S4 station in the upstream region of the sub-estuary.

943   Fig. 9. The results of the analytical solution of salinity variations along the sub-

944   estuary. a) tidal range at the mouth of the sub-estuary; b), c), and d) are subtidal

945   salinity variations at S2, S3, and S4 stations.

946   Fig. 10. Timeseries of: a) tidal range at the mouth of the sub-estuary; b) salt flux

947   at the cross-section near the mouth of the sub-estuary; c) freshwater flux at the cross-

948   section in the upstream region of the sub-estuary.

949   Fig. 11. Timeseries of water level at the confluence and surface salinity under

950   the extremely lower river discharge in the main estuary at stations of: a) S1; b) S2; c)

951   S3; d) S4.

952 Fig. 12. The results of the analytical solution of salinity variations along the sub-estuary

953   under extremely dry conditions. a) tidal range at the mouth of the sub-estuary; b),

954   c), and d) are subtidal salinity variations at S2, S3, and S4 stations.